BELLE2-NOTE-PH-2024-034
DRAFT Version 3.1
June 16, 2026

Search for $e^+e^- \to \gamma\chi_{bJ}$ ($J = 0, 1, 2$) at $\sqrt{s}$ near 10.746 GeV at Belle II

W. T. Xiong,[1,*] S. Jia,[2,†] and C. P. Shen[1,3,‡]

(The Belle II Collaboration)

[1]*Fudan University, Shanghai, China*
[2]*Southeast University, Nanjing, China*
[3]*Zhengzhou University, Henan, China*

Abstract

This note describes the study of $e^+e^- \to \gamma\chi_{bJ}$ ($J = 0, 1, 2$) at center-of-mass energies $\sqrt{s}$ = 10.653, 10.701, 10.746, and 10.804 GeV. These data were collected with the Belle II detector during special operations of the SuperKEKB collider, corresponding to 3.5, 1.6, 9.8, and 4.7 fb^{-1} of integrated luminosity, respectively. We do not find evidence for any process at each energy point. The upper limits at 90% confidence level on the Born cross sections for $e^+e^- \to \gamma\chi_{bJ}$ ($J = 0, 1, 2$) at $\sqrt{s}$ near 10.746 GeV are set.

VERSION LOG FOR MAIN CHANGES

– **Updates in Belle II Note v3.1**

- Add the source of systematic uncertainty from the signal PDF parameters. Please see Sec. 4.

– **Updates in Belle II Note v3.0:**

- The box is open and we update the open box result. Please see Sec. 3 3.5.
- Dividing systematic uncertainty into additive systematic uncertainty and multiplicative systematic uncertainty, and separately account them in the the calculations of upper limits. Please see Sec. 4.

– **Updates in Belle II Note v2.2:**

- Update the fitting procedure and add input/output check to test the stability of this fit. Please see Sec. 3 3.4.

– **Updates in Belle II Note v1.3:**

- Change the 5C fit into 4C fit for $\gamma\gamma l^+ l^-$ final states. Please see Sec. 3 3.1.
- Update the systematic uncertainties from photon reconstruction efficiency and beam-energy calibration. Please see Sec. 4.

– **Updates in Belle II Note v1.2:**

- Add systematic uncertainty due to the effect of initial state radiative photon in Sec. 4.

– **Updates in Belle II Note v1.1:**

- Remove the requirement for E_{γ_h} since the E_{γ_h} is correlated to the $M(\gamma\Upsilon(1S))$ and add selection criterion of $|\cos(\theta_{\gamma_h})| < 0.7$. Please see Sec. 3 3.1. All of the results are revised accordingly.

CONTENTS

1. INTRODUCTION

1.1. Motivation

We study the process of $e^+e^- \to \gamma\chi_{bJ}$ ($J = 0, 1, 2$) at $\sqrt{s}$ near 10.746 GeV to search for the radiative decay of $\Upsilon(10753)$, $\Upsilon(10753) \to \gamma\chi_{bJ}$ ($J = 0, 1, 2$).

The $e^+e^- \to \Upsilon(nS)\pi^+\pi^-(n = 1, 2, 3)$ cross sections at energies from 10.52 to 11.02 GeV have been measured by Belle, as shown in Fig. 1 [5]. A structure with the mass of $(10752.7 \pm 5.9^{+0.7}_{-1.1})$ MeV/c^2 and width of $(35.5^{+17.6+3.9}_{-11.3-3.3})$ MeV/c^2 was observed with a global significance of 5.2σ including systematic uncertainty. And recent measurement updates the mass of $(10756.3 \pm 2.7 \pm 0.6)$ MeV/c^2 and width of $(29.7 \pm 8.5 \pm 1.1)$ MeV/c^2 [6]. We call this state as $\Upsilon(10753)$.

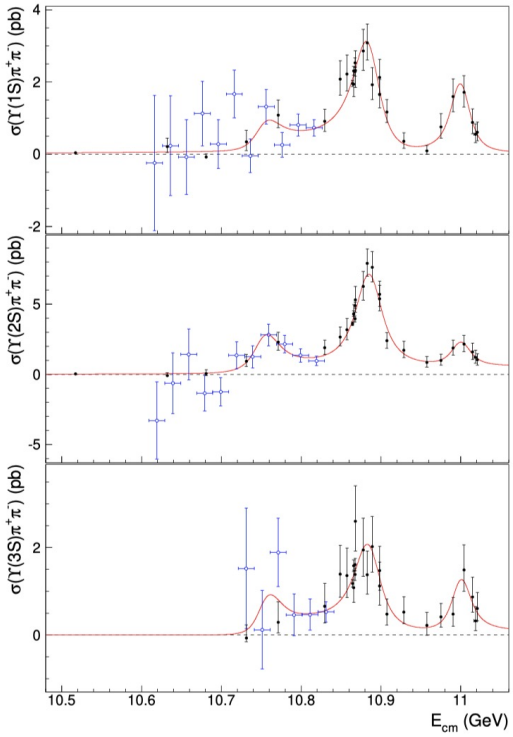

FIG. 1. Energy dependency of the $e^+e^- \to \Upsilon(nS)\pi^+\pi^-$ cross sections ($n = 1$, 2, 3 from top to bottom). The points with error bars are data; the curves are the results of the fit. Blue open dots with error bars are cross sections estimated using the ISR process in the $\Upsilon(10860)$ on-resonance data.

The $\Upsilon(10753)$ has been interpreted as a conventional bottomonium [7–16], hybrid [17, 18], or tetraquark state [19–23]. The nature of the $\Upsilon(10753)$ is unclear. To get a better knowledge of the nature of this new resonance $\Upsilon(10753)$, Belle II experiment conducted a higher statistics scan near 10.75 GeV in November 2021.

Some channels have been measured to study the nature of $\Upsilon(10753)$ energy region. In 2022, the signal of $e^+e^- \to \omega\chi_{b1}(1P)$ at $\sqrt{s} = 10.746$ GeV and evidence of $e^+e^- \to \omega\chi_{b2}(1P)$ have been observed by using full data sample near 10.746 GeV of Belle II experiment, as shown in Fig. 2 [24]. Measurements of the $e^+e^- \to B\bar{B}, B\bar{B}^*$, and $B^*\bar{B}^*$ cross sections at

10.653, 10.701, 10.746, and 10.804 GeV were performed. In the first 2 – 5 MeV above $B^*\bar{B}^*$ threshold, the $e^+e^- \to B^*\bar{B}^*$ cross section increases rapidly. This may indicate the presence of a pole close to the threshold [26]. The processes of $e^+e^- \to \omega\eta_b(1S)$ and $e^+e^- \to \omega\chi_{b0}(1P)$ were searched for using the ω meson's recoil mass with Belle II scan data at $\sqrt{s} = 10.746$ GeV [27]. No evidence for either process is found, and upper limits on the corresponding Born cross sections for $e^+e^- \to \omega\eta_b(1S)$ and $e^+e^- \to \omega\chi_{b0}(1P)$ were set to be 2.5 pb and 7.8 pb, respectively, at the 90% confidence level.

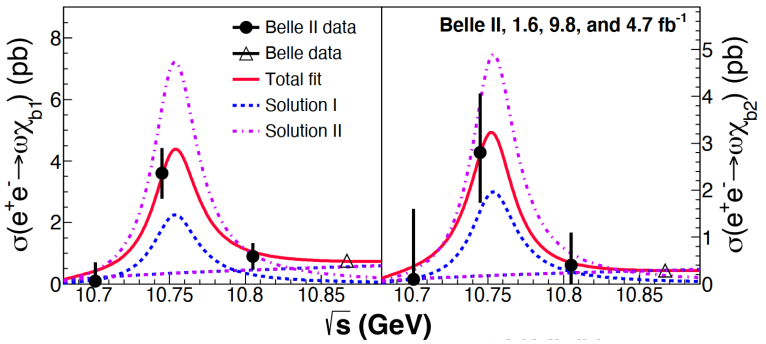

FIG. 2. The Born cross sections for $e^+e^- \to \omega\chi_{b1}$ (left) and $e^+e^- \to \omega\chi_{b2}$ (right) as a function of C.M. energy by combining the measurements of $\sigma^B(e^+e^- \to \omega\chi_{b1})$ ($\sigma^B(e^+e^- \to \omega\chi_{b2})$) from Belle at $\sqrt{s} = 10.867$ GeV [25] and Belle II at $\sqrt{s} = 10.701$, 10.746, and 10.804 GeV [24].

The radiative decay of $\Upsilon(10753)$ has not been studied experimentally. From theoretical calculations, the bottomonium with orbital angular momentum $L = 2$ decays into $\gamma\chi_{bJ}(1P)$ abundantly [28, 29]. For examples, the branching fractions for $\Upsilon_1(2^3D_1) \to \gamma\chi_{bJ}(1P)$ could be as large as a few percent, as listed in Table I [28, 29]. Therefore, if the $\Upsilon(10753)$ consists of a D-wave component, the branching fraction for $\Upsilon(10753) \to \gamma\chi_{bJ}(1P)$ is expected to be large as well. Measurements of production rates of $\Upsilon(10753) \to \gamma\chi_{bJ}(1P)$ help distinguish the nature of $\Upsilon(10753)$.

In addition, the cross section distribution for $e^+e^- \to \pi^+\pi^-\Upsilon(nS)$ [5] exhibits two closely spaced peaks corresponding to the $\Upsilon(10753)$ and $\Upsilon(10860)$, analogous to the two-peak structure observed in the cross sections for $e^+e^- \to \pi^+\pi^- J/\psi$ at $Y(4230)$ and $Y(4320)$ by BESIII [30]. Evidence for $e^+e^- \to \gamma\chi_{c1}$ and $e^+e^- \to \gamma\chi_{c2}$ was observed by BESIII with statistical significances of 3.0σ and 3.4σ, respectively, using combined data samples at $\sqrt{s}$ = 4.009, 4.230, 4.260, and 4.360 GeV. If $Y(4230)$ and $\Upsilon(10753)$ share similar internal dynamics, we would expect enhanced production of $e^+e^- \to \gamma\chi_{b1}$ and $e^+e^- \to \gamma\chi_{b2}$ near $\sqrt{s}$ = 10.746 GeV.

TABLE I. The calculated $\Upsilon_1(2^3D_1) \to \gamma\chi_{bJ}(1P)$ decay branching fractions [28, 29].

Channels	$\mathcal{B}$ from Ref. [28]	$\mathcal{B}$ from Ref. [29]
$\Upsilon_1(2^3D_1) \to \gamma\chi_{b0}(1P)$	7.7×10^{-2}	6.88×10^{-2}
$\Upsilon_1(2^3D_1) \to \gamma\chi_{b1}(1P)$	2.0×10^{-2}	2.37×10^{-2}
$\Upsilon_1(2^3D_1) \to \gamma\chi_{b2}(1P)$	5.0×10^{-4}	6.90×10^{-4}

1.2. Research method

The Born cross section for $e^+e^- \to \gamma\chi_{bJ}$ ($J = 0, 1, 2$) is calculated by:

$$\sigma^B(e^+e^- \to \gamma\chi_{bJ}) = \frac{N_{\rm fit} \times |1-\Pi|^2}{\mathcal{L} \times (\varepsilon_{e^+e^-} + \varepsilon_{\mu^+\mu^-}) \times \mathcal{B}_{\rm int} \times (1+\delta_{\rm ISR})}, \quad (1)$$

where $N_{\rm fit}$ is the signal yield of the fit combined from $\mu^+\mu^-$ and e^+e^- modes, $\mathcal{L}$ is the integrated luminosity of data sample, $\varepsilon_{e^+e^-}$ and $\varepsilon_{\mu^+\mu^-}$ are reconstruction efficiencies for $\Upsilon(1S) \to e^+e^-$ and $\Upsilon(1S) \to \mu^+\mu^-$ modes, $\mathcal{B}_{\rm int} = \mathcal{B}(\chi_{bJ} \to \gamma\Upsilon(1S)) \times \mathcal{B}(\Upsilon(1S) \to l^+l^-)$ is the product branching fraction of the intermediate states. The factor $|1-\Pi|$ is the vacuum polarization factor [33], which is listed in Table II for different energy points.

TABLE II. The values of the vacuum polarization factor at $\sqrt{s} = 10.653$, 10.701, 10.746, and 10.804 GeV.

e^+e^- center-of-mass energy	Vacuum polarization factor
10.653 GeV	0.930
10.701 GeV	0.931
10.746 GeV	0.931
10.804 GeV	0.932

The $(1+\delta_{\rm ISR})$ is the radiative correction factor, which can be calculated by [34–36]:

$$1+\delta_{\rm ISR} = \frac{\int \sigma^{\rm dressed}(s(1-x))F(x,s)dx}{\sigma^{\rm dressed}}, \quad (2)$$

where s is the square of the center-of-mass (C.M.) energy, and x is the fraction of energy carried by the ISR photon. And $F(x,s)$ is the radiative function obtain from QED calculation [34–36], which can be described as

$$F(x,s) = v(s)x^{v(s)-1}(1+\delta(s)) + x^{v(s)}(-v(s) - v(s)^2/4) + x^{v(s)+1}(v(s)/2 - \frac{3}{8}v(s)^2), \quad (3)$$

where,

$$v(s) = \frac{2\alpha}{\pi}(\log\frac{s}{m_e^2} - 1), \quad (4)$$

$$\delta(s) = \frac{\alpha}{\pi}(\frac{\pi^2}{3} - \frac{1}{2}) + \frac{3}{4}v(s) + v(s)^2(\frac{9}{32} - \frac{\pi^2}{12}), \quad (5)$$

where α is the fine structure constant, and m_e is the mass of electron. In Eq. (2), the integration limit corresponds to the $\gamma\chi_{bJ}$ mass threshold, which corresponds to the left end of $\Upsilon(10753)$ mass. The $\sigma^{\rm dressed}$ is the "dressed" cross section, and we assume

$$\sigma^{\rm dressed}(\sqrt{s}) = \frac{1}{s}, \quad (6)$$

The values of radiative correction factors of different C.M. energies and different final states are calculated, which are listed in Table III.

TABLE III. The values of radiative correction factor for $e^+e^- \to \gamma\chi_{b0}$, $e^+e^- \to \gamma\chi_{b1}$, and $e^+e^- \to \gamma\chi_{b2}$ at $\sqrt{s}$ = 10.653, 10.701, 10.746, and 10.804 GeV, respectively.

$1+\delta_{\rm ISR}$	$\sqrt{s}$ = 10.653 GeV	$\sqrt{s}$ = 10.701 GeV	$\sqrt{s}$ = 10.746 GeV	$\sqrt{s}$ = 10.804 GeV
$e^+e^- \to \gamma\chi_{b0}$	0.901	0.905	0.909	0.914
$e^+e^- \to \gamma\chi_{b1}$	0.898	0.905	0.906	0.911
$e^+e^- \to \gamma\chi_{b2}$	0.896	0.901	0.904	0.909

2. DATASET

2.1. Signal MC samples

We generate 50k signal Monte Carlo (MC) events for each energy point and each process to determine the signal line shapes and the reconstruction efficiencies. A combination of PHOKHARA [37] and EVTGEN [38] based on the release-06-00-08 is used. We use the PHOKHARA generator [37] to generate the $e^+e^- \to V\gamma_{\rm ISR}$ process at the next to leading order accuracy. And we simulate the decay chain $V \to \gamma\chi_{bJ}$ (J = 0, 1, 2) using EVTGEN generator [38]. Here the angular distribution is in phase space. And we will change the angular distribution by $1 \pm \cos^2\theta$ and take the difference in the efficiency as systematic uncertainty due to the angular distribution. For $\chi_{b0} \to \gamma\Upsilon(1S)$ decay, HLEAMP mode with parameters (1. 0. 1. 0.) is used. For $\chi_{b1} \to \gamma\Upsilon(1S)$ decay, HLEAMP mode with parameters (1. 0. 1. 0. -1. 0. -1. 0.) is used. For $\chi_{b2} \to \gamma\Upsilon(1S)$ decay, PHSP mode is used. For $\Upsilon(1S) \to l^+l^-$ decay, VLL mode is used. The effect of final-state radiation is taken into account in the simulation using the PHOTOS package.

Run-dependent signal MC samples are produced by including beam background overlaying samples. The GEANT4 [39] is used to simulate the detector response.

2.2. Generic MC samples

We use official generic MC samples at $\sqrt{s}$ near 10.746 GeV in this analysis. It corresponds to Run-dependent MC – proc13 + prompt-5S scan. The details are shown in Table IV. Besides above, we also used e^+e^- type (Bhabha) events with an integrated luminosity of 17.481 fb^{-1} from Run-dependent MC – prompt - 4S exp 20-26.

2.3. Data samples

$\Upsilon(10750)$ scan data samples from prompt reprocessing bucket#27 are used, and details are shown in Table V.

– C.M. energy: 10.653, 10.701, 10.746, and 10.804 GeV

We use the global tag of beamEnergy_bucket27_prompt [40] to correct beam energies and the C.M. energies in data.

TABLE IV. Event type and size of generic MC samples (Run-dependent MC – proc13 + prompt-5S scan).

Event type	Collected Luminosity (fb^{-1})
$u\overline{u}$	200
$d\overline{d}$	200
$s\overline{s}$	200
$c\overline{c}$	200
$\tau^+\tau^-$	1000
$e^+e^-e^+e^-$	100
$e^+e^-\mu^+\mu^-$	100
B^+B^-	200
$B^0\overline{B^0}$	200

TABLE V. The luminosity, experiment number, and run range of $\Upsilon(10750)$ scan data samples.

Energy (GeV)	Collected luminosity (fb^{-1})	Exp No.	Run range
10.653	3.52±0.01	21	83-186
10.701	1.63±0.01	21	192-235
10.746	9.82±0.02	21	245-490
10.804	4.69±0.02	21	507-572

3. ANALYSIS OF $\Upsilon(10753) \to \gamma\chi_{bJ}$ (J = 0, 1, 2)

3.1. Selection criteria

The following selection criteria aim to select signal and reduce background as efficiently as possible. The final states for $e^+e^- \to \gamma\chi_{bJ}$ (J = 0, 1, 2) are $\gamma\gamma l^+l^-$, where l represents e or μ.

- Charged tracks

  All charged tracks are required to originate from the vicinity of the interaction point (IP). We require $|dr| < 1$ cm and $|dz| < 3$ cm, where dr and dz are transverse and longitudinal distances in respect to IP. Figure 3 shows the distributions of $|dr|$ and $|dz|$ from signal MC and data samples at $\sqrt{s} = 10.746$ GeV. Please note that all "Data" in the figures in this chapter are real data samples at $\sqrt{s} = 10.746$ GeV. The red arrows show the requirements of $|dr| < 1$ cm and $|dz| < 3$ cm.

  - For the lepton pairs l^+l^- used to reconstruct $\Upsilon(1S)$, we require the electronID_noSVD_noTOP ($\mathcal{R}_e = \frac{\mathcal{L}_e}{\mathcal{L}_e+\mathcal{L}_\mu+\mathcal{L}_\pi+\mathcal{L}_K+\mathcal{L}_p+\mathcal{L}_d}$) > 0.9 in the e^+e^- mode and muonID_noSVD ($\mathcal{R}_\mu = \frac{\mathcal{L}_\mu}{\mathcal{L}_e+\mathcal{L}_\mu+\mathcal{L}_\pi+\mathcal{L}_K+\mathcal{L}_p+\mathcal{L}_d}$) > 0.9 in the $\mu^+\mu^-$ mode. Figure 4 shows the distributions of electronID_noSVD_noTOP and muonID_noSVD from signal MC and data samples at $\sqrt{s} = 10.746$ GeV. The red arrows show the requirements of electronID_noSVD_noTOP > 0.9 and muonID_noSVD > 0.9.

  - The number of good charged tracks is required to be two to suppress background.

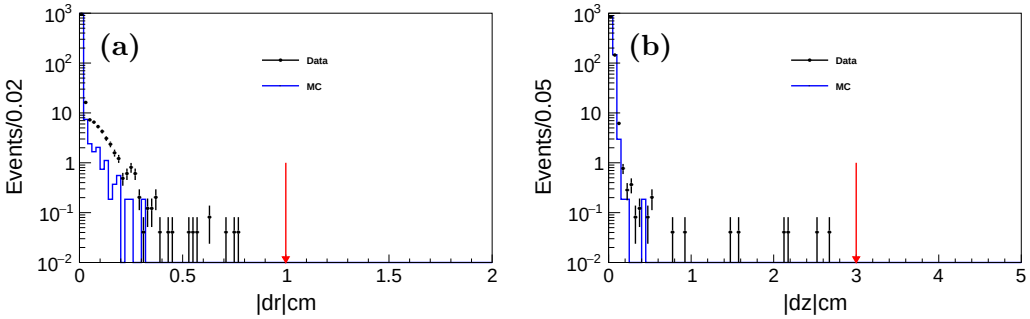

FIG. 3. Distributions of (a) $|dr|$ and (b) $|dz|$ from signal MC and data samples at $\sqrt{s} = 10.746$ GeV.

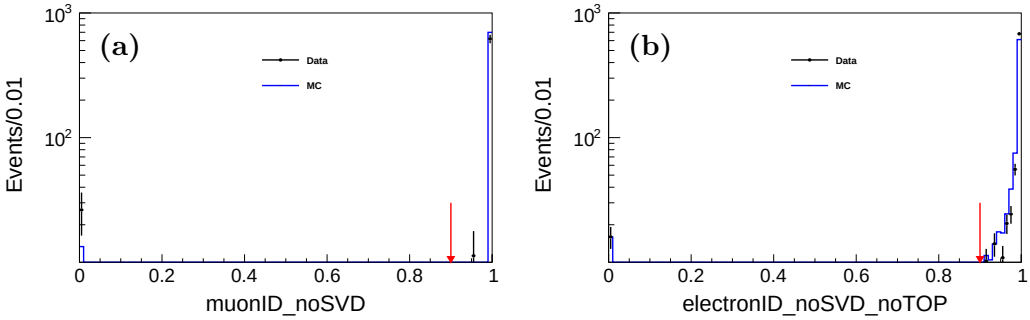

FIG. 4. Distributions of (a) muonID_noSVD ($\mathcal{R}_\mu$) and (b) electronID_noSVD_noTOP ($\mathcal{R}_e$) from signal MC and data samples at $\sqrt{s} = 10.746$ GeV.

Figure 5 shows the numbers of charged tracks ($N_{\rm trk}$) from signal MC and data sample at $\sqrt{s} = 10.746$ GeV.

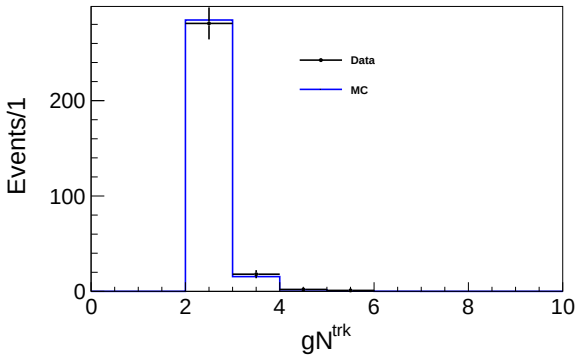

FIG. 5. Distributions of the numbers of good charged tracks ($N_{\rm trk}$) from signal MC and data samples at $\sqrt{s} = 10.746$ GeV.

- Photons

There are two photons in $e^+e^- \to \gamma\chi_{bJ}$ ($J = 0, 1, 2$) final states. We require E9/E21

> 0.8 for all the photons, where the E9/E21 is a ratio of energies in the inner 3×3 crystals and 5×5 crystals around the central crystal without corners. The photon from χ_{bJ} ($J = 0, 1, 2$) decay has lower energy, thus is remarked as γ_l. The photon in $e^+e^- \to \gamma\chi_{bJ}$ ($J = 0, 1, 2$) has higher energy, thus is remarked as γ_h. Thus, we have $e^+e^- \to \gamma_h\chi_{bJ}$, $\chi_{bJ} \to \gamma_l\Upsilon(1S)$, and $\Upsilon(1S) \to \ell^+\ell^-$.

Figure 6 shows the E_{γ_h} distributions in $e^+e^- \to \gamma_h\chi_{bJ}(\to \gamma_l\Upsilon(1S))$ ($J = 0, 1, 2$) from signal MC samples at $\sqrt{s} = 10.746$ GeV.

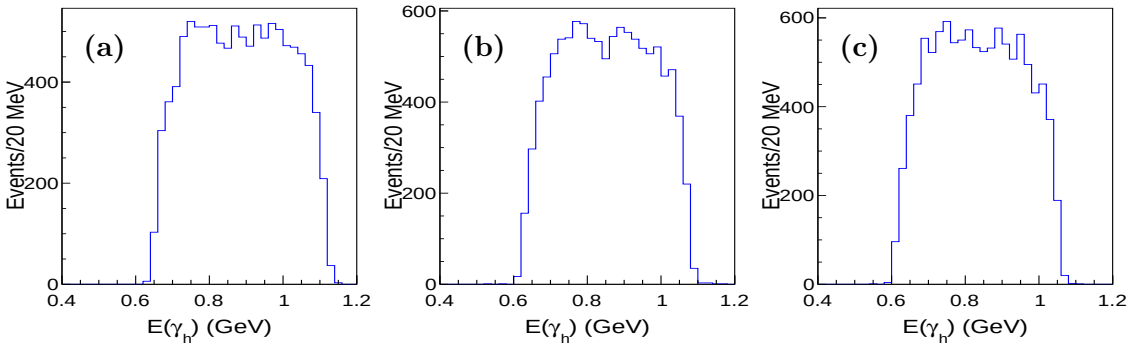

FIG. 6. The E_{γ_h} distributions in (a) $e^+e^- \to \gamma_h\chi_{b0}$, (b) $e^+e^- \to \gamma_h\chi_{b1}$, and (c) $e^+e^- \to \gamma_h\chi_{b2}$ from signal MC samples at $\sqrt{s} = 10.746$ GeV.

Figure 7 shows the E_{γ_l} distributions in $e^+e^- \to \gamma_h\chi_{bJ}(\to \gamma_l\Upsilon(1S))$ ($J = 0, 1, 2$) from signal MC samples at $\sqrt{s} = 10.746$ GeV.

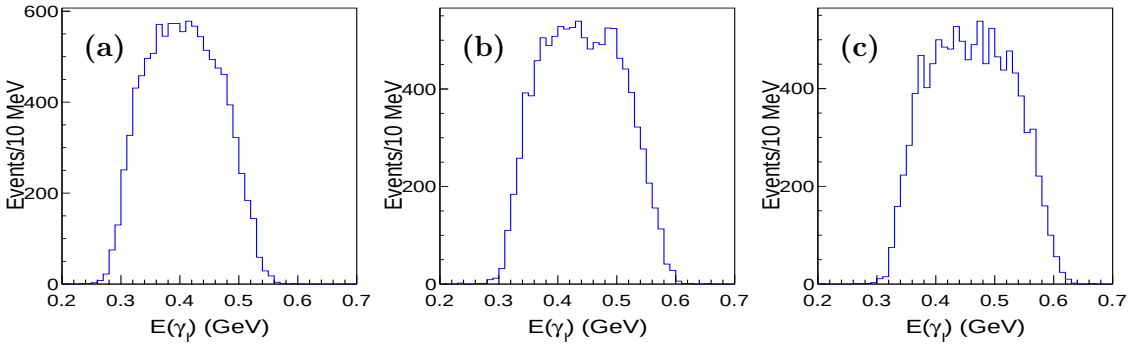

FIG. 7. The E_{γ_l} distributions in (a) $e^+e^- \to \gamma_h\chi_{b0}$, (b) $e^+e^- \to \gamma_h\chi_{b1}$, and (c) $e^+e^- \to \gamma_h\chi_{b2}$ from signal MC samples at $\sqrt{s} = 10.746$ GeV.

Figure 8 shows the scattering plots of the $E^*_{\gamma_h}$ (the energy of γ_h in e^+e^- center-of-mass frame) versus $M(\gamma\Upsilon(1S))$ in $e^+e^- \to \gamma_h\chi_{b0}$. The $E^*_{\gamma_h}$ is highly correlated with the $M(\gamma\Upsilon(1S))$. The selected region of $M(\gamma\Upsilon(1S))$ equals to the application of requirement of E_{γ_h} to some extend. Thus, we just take a loose "protective" selection criterion of $E_{\gamma_h} > 50$ MeV.

We optimize the E_{γ_l} by maximizing the FOM parameter $\frac{\varepsilon}{\frac{3}{2}+\sqrt{B}}$ [41], where ε is the efficiency from signal MC samples and B is the number of background events from

normalized generic MC samples. Figure 9 shows the FOM parameter distributions of E_{γ_l} for $\mu^+\mu^-$ mode and e^+e^- mode in $e^+e^- \to \gamma_h\chi_{b0}(\to \gamma_l\Upsilon(1S))$.

From Figure 18, the data sidebands are basically consistent with generic MC. If we use the $\Upsilon(1S)$ mass sidebands for estimating the number of background events, the optimized results do not change.

Please note that we identify the signal via the same $M(\gamma_l\Upsilon(1S))$ distribution for different $\chi_{b0,b1,b2}$ decays. Thus, for different $\chi_{b0,b1,b2}$ decays, the requirements should be the same. Here, we chose the $e^+e^- \to \gamma\chi_{b0}$ channel to optimize the E_{γ_l} requirement to obtain the most conservative result. We require $E_{\gamma_l} > 280$ MeV for $\mu^+\mu^-$ mode and $E_{\gamma_l} > 290$ MeV for e^+e^- mode, respectively, at each energy point.

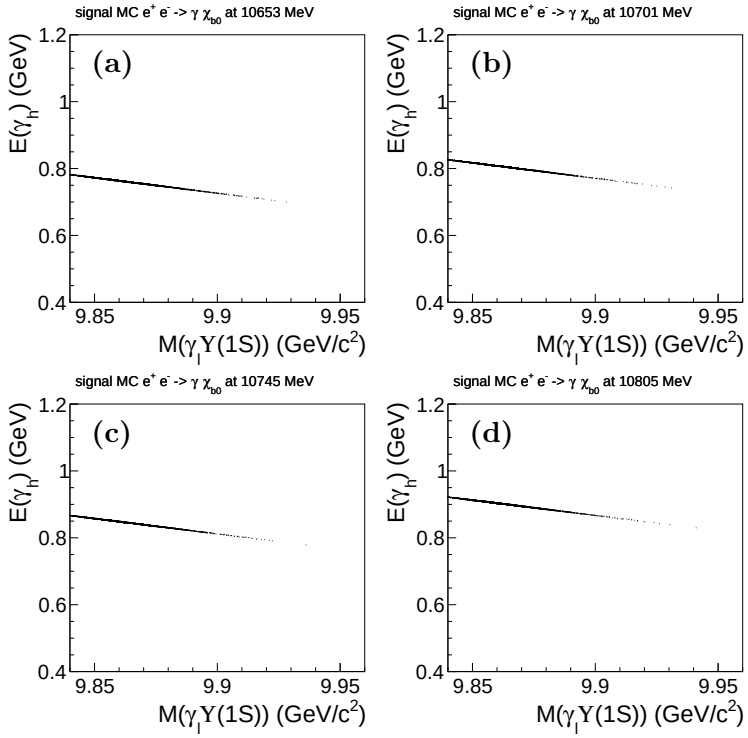

FIG. 8. The scattering plots of the $E^*_{\gamma_h}$ (the energy of γ_h in e^+e^- center-of-mass frame) versus $M(\gamma\Upsilon(1S))$ from MC simulated $e^+e^- \to \gamma_h\chi_{b0}(\to \gamma_l\Upsilon(1S))$ at (a) $\sqrt{s} = 10.653$ GeV, (b) $\sqrt{s} = 10.701$ GeV, (c) $\sqrt{s} = 10.746$ GeV, and (d) $\sqrt{s} = 10.804$ GeV, respectively.

- Helicity angle

Figure 10 shows the distributions of the absolute value of the cosine of helicity angle of γ_h from generic MC sample at $\sqrt{s} = 10.746$ GeV. Here, the helicity angle is the polar angle of γ_h in the e^+e^- center-of-mass frame. More Bhabha background events are accumulated in the higher side. We optimize the $|\cos(\theta_{\gamma_h})|$ for the e^+e^- mode by maximizing the FOM parameter $\frac{\varepsilon}{\frac{3}{2}+\sqrt{B}}$ [41], where ε is the efficiency from signal MC samples and B is the number of background events from normalized generic MC samples. Figure 11 shows the distributions of the cosine value of helicity angle of γ_h from MC simulated $e^+e^- \to \gamma_h\chi_{b0}(\to \gamma_l\Upsilon(1S))$ assuming $1+\cos^2(\theta_{\gamma_h})$ distribution and

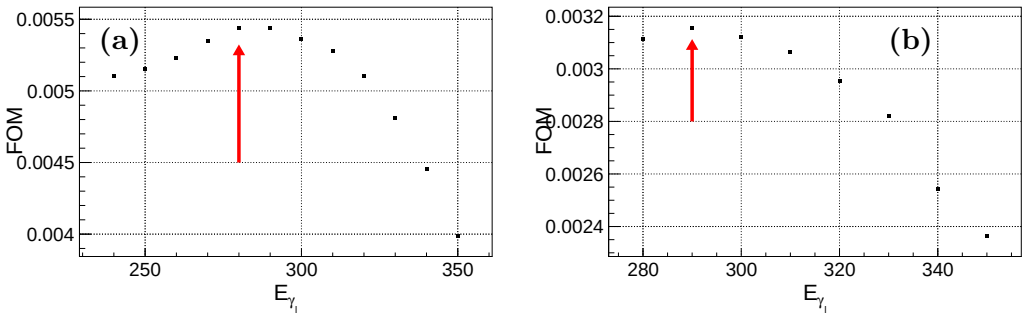

FIG. 9. The FOM parameter distributions of E_{γ_l} from MC simulated $e^+e^- \to \gamma_h\chi_{b0}(\to \gamma_l\Upsilon(1S))$ of (a) $\mu^+\mu^-$ final state and (b) e^+e^- final state at $\sqrt{s} = 10.746$ GeV.

$1-\cos^2(\theta_{\gamma_h})$ distribution at $\sqrt{s} = 10.746$ GeV. Figure 12 shows the FOM parameter distributions of $|\cos(\theta_{\gamma_h})|$ for $1+\cos^2(\theta_{\gamma_h})$ distribution and $1-\cos^2(\theta_{\gamma_h})$ distribution. We require $|\cos(\theta_{\gamma_h})| < 0.7$ in the e^+e^- mode to suppress the Bhabha background events.

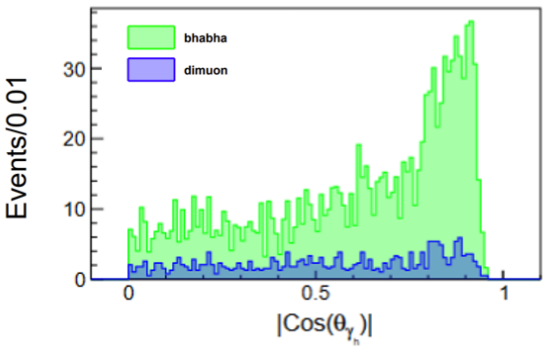

FIG. 10. The distributions of the absolute value of the cosine of helicity angle of γ_h from generic MC sample at $\sqrt{s} = 10.746$ GeV.

- $\Upsilon(1S) \to e^+e^-$

  In order to consider the effect of bremsstrahlung or final-state radiation,

- $\Upsilon(1S)$ mass

  The invariant mass distributions of lepton pairs are shown in Fig. 13. We require the mass of lepton pair larger than 9.44 GeV/c^2 and smaller than 9.49 GeV/c^2 to select $\Upsilon(1S)$ signal candidates. The red lines in Fig. 13 show the $\Upsilon(1S)$ signal region ($9.44\ \mathrm{GeV}/c^2 < M(l^+l^-) < 9.49\ \mathrm{GeV}/c^2$), and the green lines show the $\Upsilon(1S)$ mass sidebands ($9.34\ \mathrm{GeV}/c^2 < M(l^+l^-) < 9.39\ \mathrm{GeV}/c^2$ and $9.54\ \mathrm{GeV}/c^2 < M(l^+l^-) < 9.59\ \mathrm{GeV}/c^2$).

  We optimize the $\Upsilon(1S)$ signal region by maximizing the FOM parameter $\frac{\varepsilon}{\frac{3}{2}+\sqrt{B}}$ [41], where ε is the efficiency and B is the number of background events from normalized

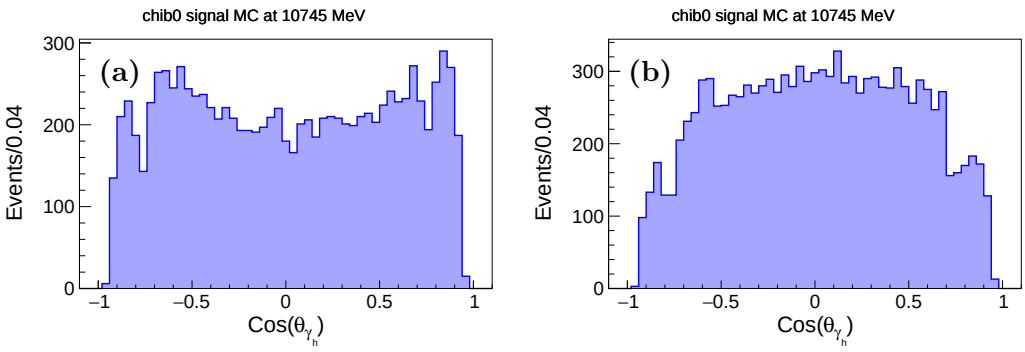

FIG. 11. The distributions of the cosine value of helicity angle of γ_h from MC simulated $e^+e^- \to \gamma_h\chi_{b0}(\to \gamma_l\Upsilon(1S))$ assuming (a) $1+\cos^2(\theta_{\gamma_h})$ distribution and (b) $1-\cos^2(\theta_{\gamma_h})$ distribution at $\sqrt{s}$ = 10.746 GeV.

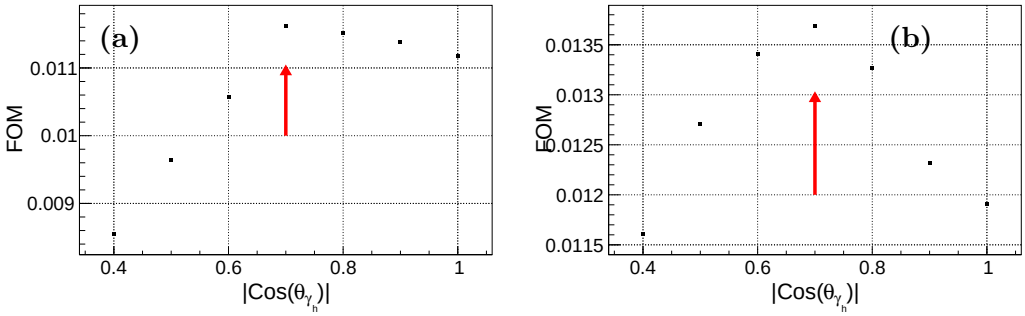

FIG. 12. The FOM parameter distributions of $|\cos(\theta_{\gamma_h})|$ from MC simulated $e^+e^- \to \gamma_h\chi_{b0}(\to \gamma_l\Upsilon(1S))$ of (a) $1+\cos^2(\theta_{\gamma_h})$ distribution and (b)$1-\cos^2(\theta_{\gamma_h})$ distribution at $\sqrt{s}$ = 10.746 GeV.

generic MC samples. Table VI shows the values of the FOM parameters for different $\Upsilon(1S)$ signal regions, and we require the mass of lepton pair larger than 9.44 GeV and smaller than 9.49 GeV according to the maximum value of FOM.

- We perform a four momentum constraint (4C) fit using KFIT for $\gamma\gamma l^+l^-$ final states to suppress the background with one or more additional or missing particles in the final

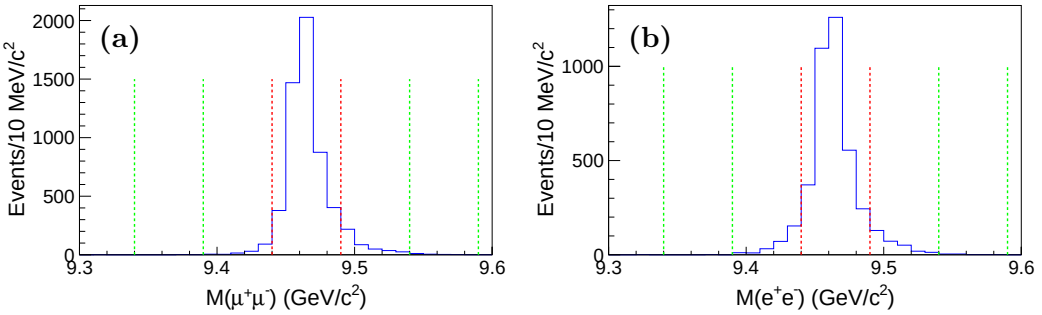

FIG. 13. Distributions of lepton pair mass from signal MC samples for (a) $\mu^+\mu^-$ final state and (b) e^+e^- final state at $\sqrt{s}$ = 10.746 GeV.

TABLE VI. The values of FOM parameters with different $\Upsilon(1S)$ mass regions.

$M(l^+l^-)$ region (GeV/c^2)	FOM value
$[9.45, 9.48]$	0.0062
$[9.44, 9.49]$ (nominal)	0.0065
$[9.43, 9.50]$	0.0063
$[9.42, 9.51]$	0.0062
$[9.41, 9.52]$	0.0061
$[9.40, 9.53]$	0.0060
$[9.39, 9.54]$	0.0059

states and improve the mass resolutions, where four-momenta of the final state system are constrained to the initial e^+e^- C.M. system. Specially, we use the ($M(\gamma\Upsilon(1S))$ - $M(\Upsilon(1S))$ + 9.46) instead of $M(\gamma\Upsilon(1S))$ to draw the invariant mass distribution of $\gamma\Upsilon(1S)$ to improve the mass resolution. If there are multiple combinations in one event, the one with the smallest 4C fit χ^2 is retained. Here the percentage of multiple candidates per event is 2.2% in data. We optimize the χ^2_{4C} by maximizing the FOM parameter $\frac{\varepsilon}{\frac{3}{2}+\sqrt{B}}$ [41], where ε is the efficiency B is the number of background events from normalized generic MC samples.

Figure 14 shows the FOM parameter distribution of 4C fit χ^2 and the distributions of 4C fit χ^2 from signal MC and data samples at $\sqrt{s} = 10.746$ GeV. The red arrows show the requirement of $\chi^2_{4C} < 30$.

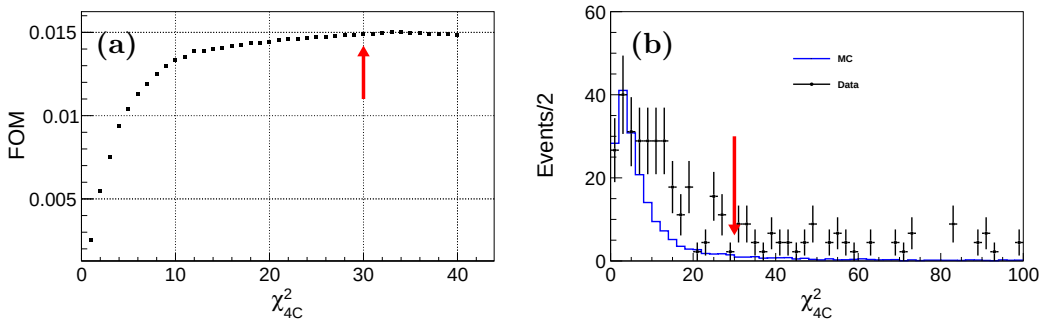

FIG. 14. The (a) FOM parameter distribution of 4C fit χ^2_{4C} and (b) 4C fit χ^2_{4C} distributions from signal MC and data samples at $\sqrt{s} = 10.746$ GeV.

3.2. The study of signal MC samples

3.2.1. *Distribution from signal MC samples*

After applying all selection requirements, the invariant mass distributions of $\gamma\Upsilon(1S)$ from signal MC samples in $e^+e^- \to \gamma\chi_{bJ}$ ($J = 0, 1, 2$) at $\sqrt{s} = 10.653$, 10.701, 10.746, and 10.804 GeV are shown in Figs. 15, 16, and 17, respectively. Here we use a Crystal Ball (CB) function ($\mathcal{F}_{\rm CB}(M; \mu, \sigma, \alpha, n)$) [42] combined with a Gaussian function to describe the χ_{bJ} signal shapes. All parameters in CB and Gaussian functions are free.

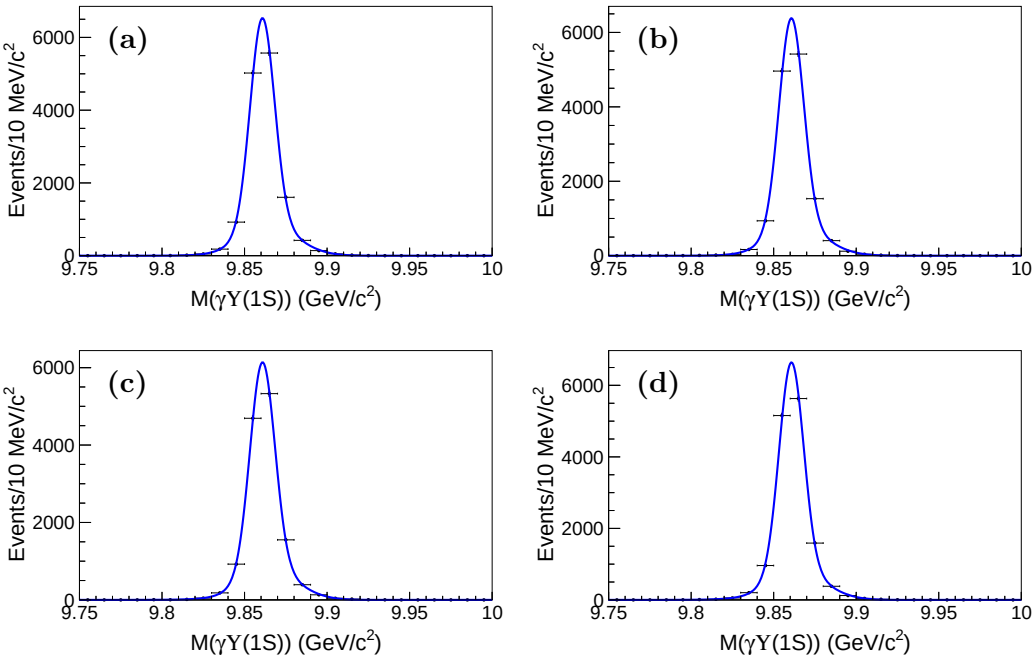

FIG. 15. The invariant mass spectra of $\gamma\Upsilon(1S)$ from MC simulated $e^+e^- \to \gamma\chi_{b0}$ at (a) $\sqrt{s} = 10.653$ GeV, (b) $\sqrt{s} = 10.701$ GeV, (c) $\sqrt{s} = 10.746$ GeV, and (d) $\sqrt{s} = 10.804$ GeV, respectively.

Table VII and table VIII show the reconstruction efficiency from signal MC samples from e^+e^- mode and $\mu^+\mu^-$ mode, respectively.

TABLE VII. Reconstruction efficiency (%) from signal MC samples of e^+e^- mode.

Energy (GeV)	$\gamma\chi_{b0}$	$\gamma\chi_{b1}$	$\gamma\chi_{b2}$
10.653	21.5	22.3	21.2
10.701	21.4	21.7	21.9
10.746	21.6	21.2	21.8
10.804	22.2	22.4	22.8

3.3. The study of generic MC samples

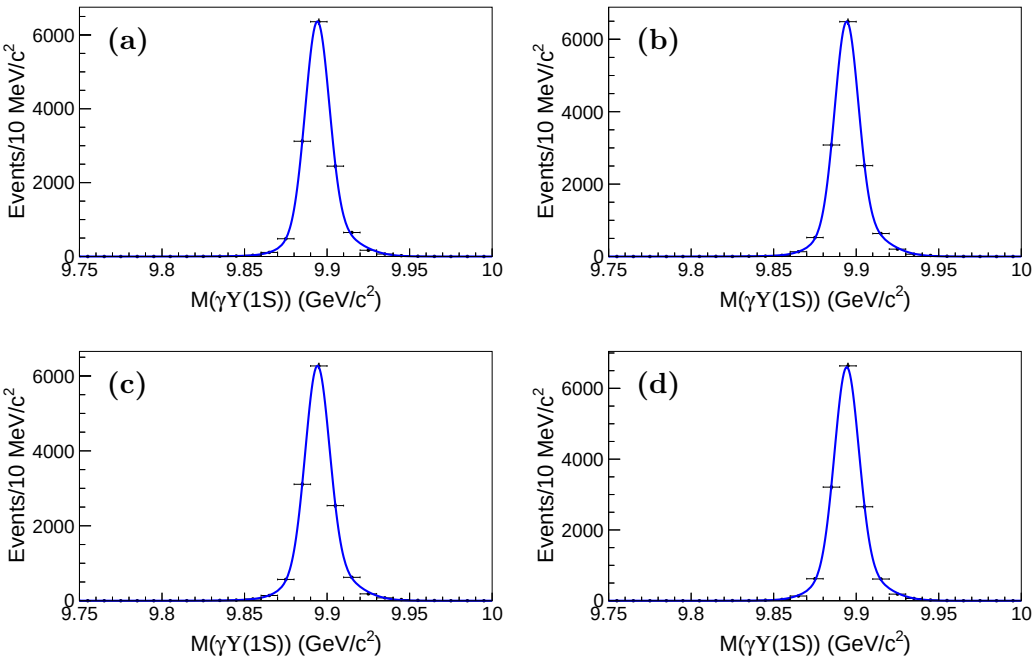

FIG. 16. The invariant mass spectra of $\gamma\Upsilon(1S)$ from MC simulated $e^+e^- \to \gamma\chi_{b1}$ at (a) $\sqrt{s} =$ 10.653 GeV, (b) $\sqrt{s} = 10.701$ GeV, (c) $\sqrt{s} = 10.746$ GeV, and (d) $\sqrt{s} = 10.804$ GeV, respectively.

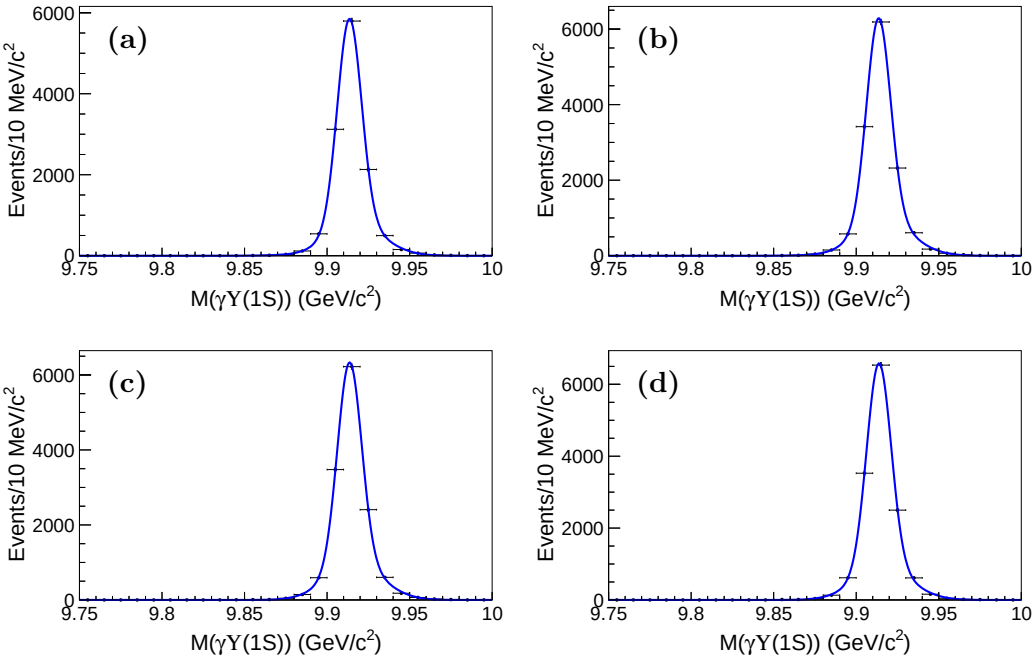

FIG. 17. The invariant mass spectra of $\gamma\Upsilon(1S)$ from MC simulated $e^+e^- \to \gamma\chi_{b2}$ at (a) $\sqrt{s} =$ 10.653 GeV, (b) $\sqrt{s} = 10.701$ GeV, (c) $\sqrt{s} = 10.746$ GeV, and (d) $\sqrt{s} = 10.804$ GeV, respectively.

TABLE VIII. Reconstruction efficiency (%) from signal MC samples of $\mu^+\mu^-$ mode.

Energy (GeV)	$\gamma\chi_{b0}$	$\gamma\chi_{b1}$	$\gamma\chi_{b2}$
10.653	36.1	35.3	34.1
10.701	34.6	35.1	34.1
10.746	35.6	36.1	35.8
10.804	36.1	36.6	36.4

After applying all of the above selection criteria, Figure 18 shows the invariant mass distributions of $\gamma\Upsilon(1S)$ from normalized generic MC samples at $\sqrt{s} = 10.653$, 10.701, 10.746, and 10.804 GeV, respectively. The remaining backgrounds are mainly from Bhabha and dimuon processes. No peaking backgrounds are found.

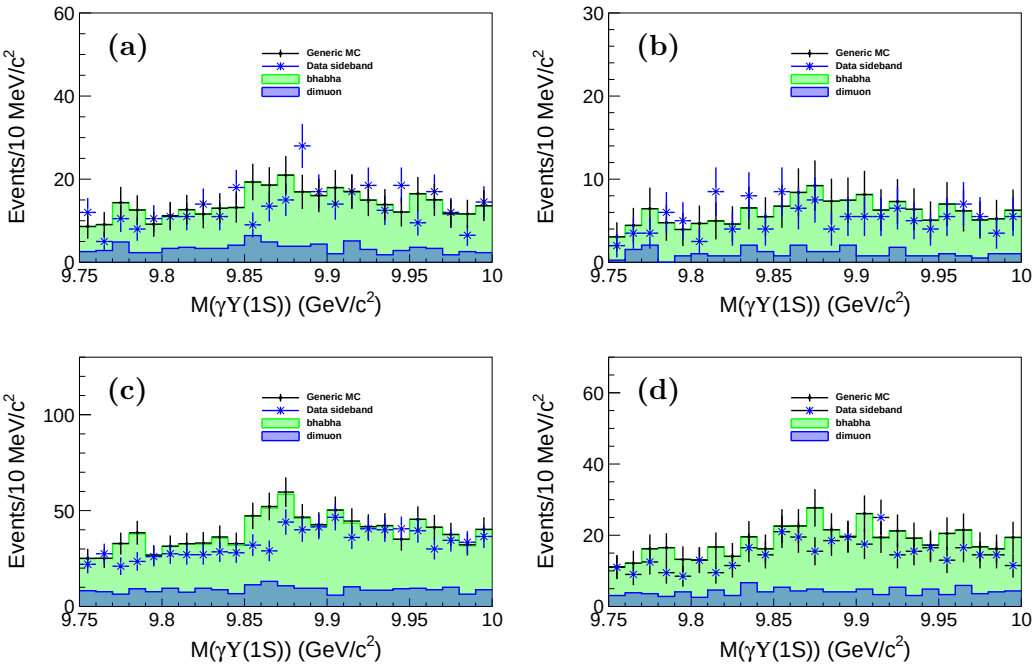

FIG. 18. The invariant mass spectra of $\gamma\Upsilon(1S)$ from normalized generic MC samples and normalized $\Upsilon(1S)$ mass sidebands in data at (a) $\sqrt{s} = 10.653$ GeV, (b) $\sqrt{s} = 10.701$ GeV, (c) $\sqrt{s} = 10.746$ GeV, and (d) $\sqrt{s} = 10.804$ GeV. The black points with error bars are generic MC. The blue histograms show the dimuon process. And the green histograms show the Bhabha process.The blue points with error bars are $\Upsilon(1S)$ mass sidebands in data.

3.4. Signal extraction

To study the strategies of the fits to the invariant mass spectra of $\gamma\Upsilon(1S)$, we combine the data sideband samples and signal MC samples to expected signal yields.

The unbinned extended maximum-likelihood fits are performed. Here, we simultaneous fit $\Upsilon(1S) \to \mu^+\mu^-$ and $\Upsilon(1S) \to e^+e^-$ mode. In the simultaneous fit, the ratio of yields

between $\mu^+\mu^-$ and e^+e^- channel is fixed according to the efficiency. The χ_{bJ} signal shape is described by a combination of Crystal Ball (CB) and Gaussian functions. All of the parameters in CB and Gaussian function are fixed according to signal MC simulations. A second order Chebyshev polynomial will be used to describe the background. The parameters in the polynomial function are floated.

The stability of the fits with this procedure has been tested. Assuming the Born cross section for $e^+e^- \to \gamma\chi_{bJ}$ (J = 0, 1, 2) at $\sqrt{s}$ = 10.653, 10.701, 10.746, and 10.804 GeV of 1 pb, we generate signal MC samples. Figure 19 shows the combined samples and the fit results at $\sqrt{s}$ = 10.653, 10.701, 10.746, and 10.804 GeV. The comparisons between inputs and outputs on the Born cross section are listed in Table IX. The input and output results on the signal yields are consistent within $\pm 1\sigma$.

TABLE IX. Comparisons of the values of inputs and outputs on the Born cross section (pb) from the fits at $\sqrt{s}$ = 10.653, 10.701, 10.746, and 10.804 GeV.

Energy (GeV)		$\gamma\chi_{b0}$	$\gamma\chi_{b1}$	$\gamma\chi_{b2}$
10.653	Input	1.0	1.0	1.0
	Output	5.1 ± 4.3	0.9 ± 0.3	1.3 ± 0.5
10.701	Input	1.0	1.0	1.0
	Output	4.3 ± 5.3	1.2 ± 0.4	0.7 ± 0.7
10.746	Input	1.0	1.0	1.0
	Output	2.4 ± 2.3	1.1 ± 0.2	1.1 ± 0.2
10.804	Input	1.0	1.0	1.0
	Output	1.5 ± 1.5	0.9 ± 0.2	0.8 ± 0.3

3.5. The Study of data samples

After the application of the above requirements, the $M(l^+l^-)$ distribution from a combined $\sqrt{s}$ = 10.653, 10.701, 10.746, and 10.804 GeV data sample is shown in Fig. 20.The red dash lines in Fig. 20 show the $\Upsilon(1S)$ signal region (9.44 GeV/c^2 < $M(l^+l^-)$ < 9.49 GeV/c^2). No clear $\Upsilon(1S)$ signal is observed. With the requirement of the $\Upsilon(1S)$ signal region, the $\gamma\Upsilon(1S)$ invariant mass distributions from data samples at $\sqrt{s}$ = 10.653, 10.701, 10.746, and 10.804 GeV are shown in Fig. 21. The $\gamma\Upsilon(1S)$ invariant mass distributions from a combined $\sqrt{s}$ = 10.653, 10.701, 10.746, and 10.804 GeV data sample are shown in Fig. 22.

We perform unbinned extended maximum-likelihood fits to $\gamma\Upsilon(1S)$ invariant mass distributions to extract signal yields. Here, we simultaneously fit $\Upsilon(1S) \to \mu^+\mu^-$ and $\Upsilon(1S) \to e^+e^-$ modes. In the simultaneous fit, the ratio of yields between $\mu^+\mu^-$ and e^+e^- channels is fixed according to their respective reconstruction efficiencies (we assume the same branching fraction of $(2.46 \pm 0.04) \times 10^{-2}$ for $\Upsilon(1S) \to e^+e^-$ and $\Upsilon(1S) \to \mu^+\mu^-$ [43]). The probability density function (PDF) of χ_{bJ} signal is modeled as a sum of a Crystal Ball function [42] and a Gaussian function, sharing a common mean. The mean is fixed to the nominal χ_{bJ} mass value from Particle Data Group [43], while the remaining parameters are derived from simulation. To account for data-simulation discrepancies, the photon energy in simulated events is smeared according to the measured photon energy resolution scale factor, 1.01 ± 0.01,

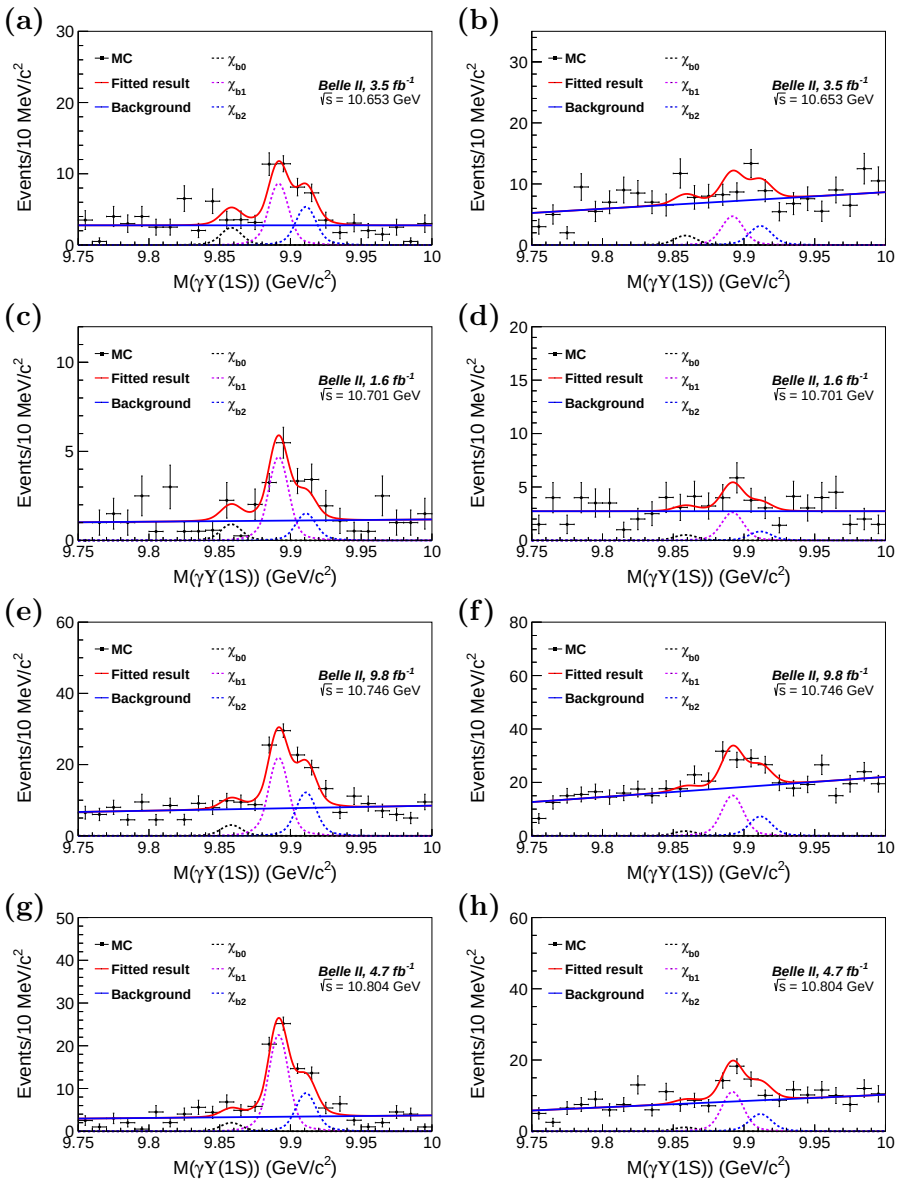

FIG. 19. The simultaneous fitted results to $M(\gamma\Upsilon(1S))$ distributions for combined signal MC samples and data sideband samples in (left) $\mu^+\mu^-$ and (right) e^+e^- modes at $\sqrt{s}$ = (a, b) 10.653, (c, d) 10.701, (e, f) 10.746, and (g, h) 10.804 GeV, respectively. Here the dots with error bars are the combined signal MC samples and data sideband samples. The red curves show the fitted results. The blue cyan curves show the total backgrounds. The black, purple, and blue dashed curves show the χ_{b0}, χ_{b1}, and χ_{b2} signals.

obtained from the $\pi^0 \to \gamma\gamma$ control sample [51]. A second order Chebyshev polynomial will be used to describe the background. The parameters in the polynomial function are floated.

We calculate the signal significance according to

$$\sqrt{-2\ln(\mathcal{L}_0/\mathcal{L}_{\rm max})}, \tag{7}$$

where $\mathcal{L}_0$ and $\mathcal{L}_{\rm max}$ are the maximized likelihoods without and with the signal, respectively.

The signal yields at each energy point are listed in Table X. No significant χ_{bJ} (J = 0, 1,

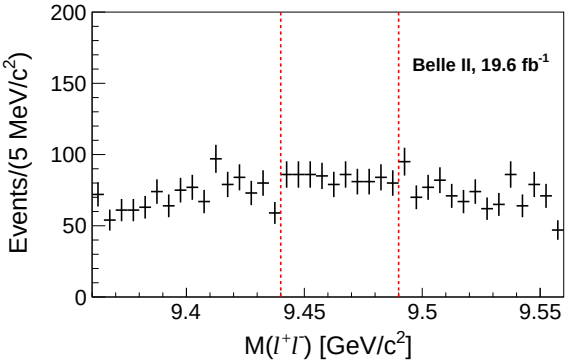

FIG. 20. The invariant mass spectrum of l^+l^- from a combined $\sqrt{s}$ = 10,653, 10.701, 10.746, and 10.804 GeV data sample. The red dash lines show the signal region (9.44 GeV/c^2 < $M(l^+l^-)$ < 9.49 GeV/c^2).

2) signal was found. We thus compute 90% C.L. upper limits $x^{\rm UL}$ on the signal yields and Born cross sections by solving the equation

$$\int_0^{x^{\rm UL}} \mathcal{L}(x)dx / \int_0^{+\infty} \mathcal{L}(x)dx = 0.90, \tag{8}$$

where x is the assumed signal yield or Born cross section, and $\mathcal{L}(x)$ is the corresponding maximized likelihood of the fit to the assumption. TThe upper limits on the signal yields including systematic uncertainties (discussed below) are listed in Table X.

The upper limits on the Born cross sections are calculated according to Eq.(1), the values used to determine the Born cross sections as well as the upper limits on the Born cross sections including systematic uncertainties are listed in Table X.

4. SYSTEMATIC UNCERTAINTY

The systematic uncertainties in the cross-section measurements of $e^+e^- \to \gamma\chi_{bJ}$ include detection efficiency uncertainties (tracking, particle ID, photon reconstruction), trigger simulation, MC statistics, branching fractions of intermediate states, integrated luminosity, angular distributions, beam-energy calibration, the radiative correction factor, the signal PDF parameters, and fit model. The systematic uncertainties from the signal PDF parameters and fit model are additive. The other sources of systematic uncertainties are multiplicative, which are listed in Table XII.

- Detection efficiency

  (a) Tracking

  For a lepton track, a systematic uncertainty of 0.3% per track is included [44].

  (b) Particle ID

  In our event selection, we only require at least one lepton to be identified. Consequently, the lepton identification efficiency is so high (> 99%) that the corresponding systematic uncertainty is negligible.

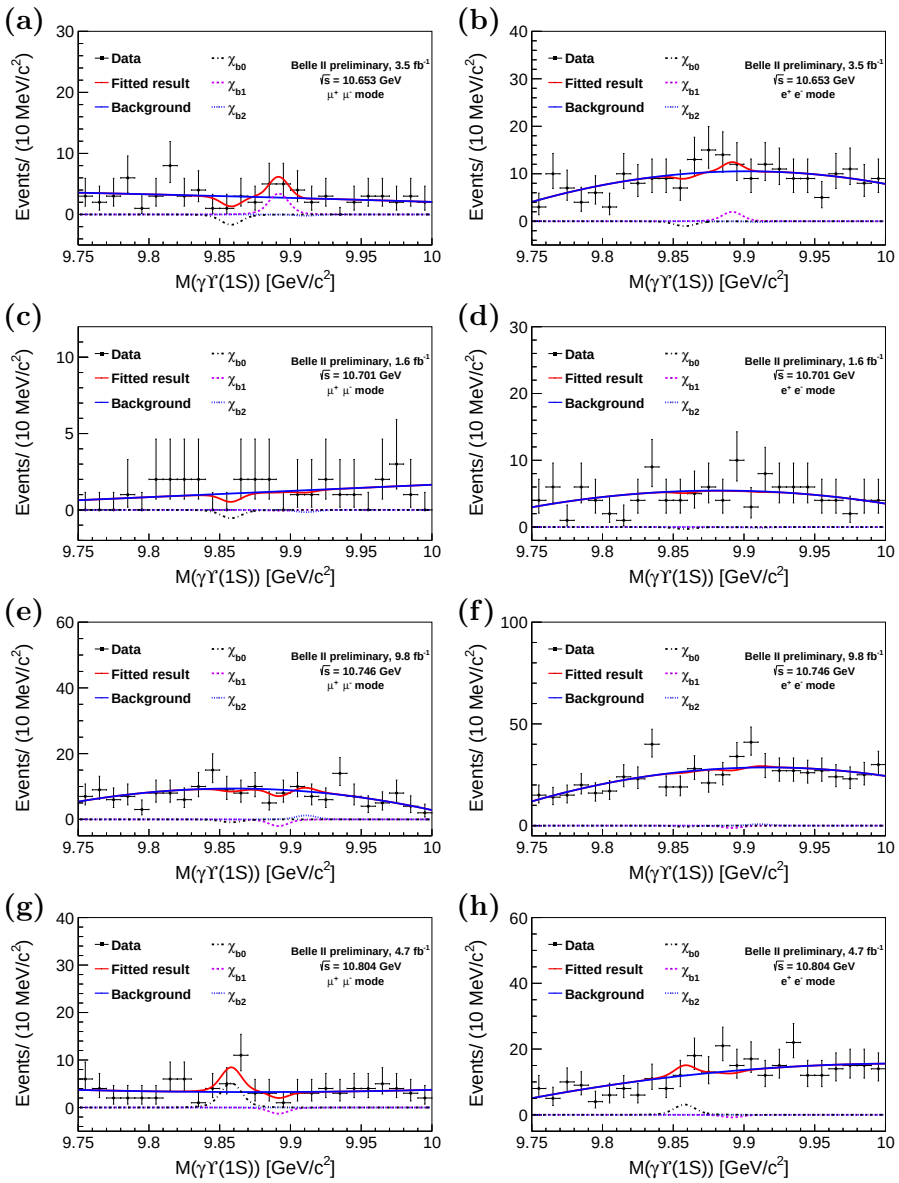

FIG. 21. The simultaneous fitted results to $M(\gamma\Upsilon(1S))$ distributions from data samples in (left) $\mu^+\mu^-$ and (right) e^+e^- modes at $\sqrt{s}$ = (a, b) 10.653, (c, d) 10.701, (e, f) 10.746, and (g, h) 10.804 GeV, respectively. Here the dots with error bars are the data samples. The red curves show the fitted results. The blue cyan curves show the total backgrounds. The black, purple, and blue dashed curves show the χ_{b0}, χ_{b1}, and χ_{b2} signals.

(c) Photon reconstruction

The Data/MC ratio of photon reconstruction efficiency of the Belle II calorimeter using di-muon events has been studied [49]. By weighting events in different regions of (θ, ϕ, E), we find the Data/MC ratio is (97.0±1.1)% for γ_l and (98.2±0.7)% for γ_h. The corrections are applied to the efficiencies of signal MC. The uncertainties on corrections are included as systematic uncertainties due to photon reconstruction.

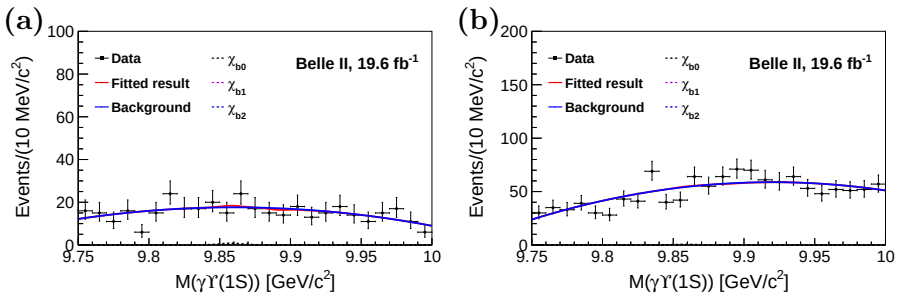

FIG. 22. The simultaneous fitted results to $M(\gamma\Upsilon(1S))$ distributions from a combined $\sqrt{s}$ = 10,653, 10.701, 10.746, and 10.804 GeV data sample in (a) $\mu^+\mu^-$ and (b) e^+e^- modes. Here the dots with error bars are the data samples. The red curves show the fitted results. The blue cyan curves show the total backgrounds. The black, purple, and blue dashed curves show the χ_{b0}, χ_{b1}, and χ_{b2} signals.

TABLE X. The values used to determine the Born cross sections for $e^+e^- \to \gamma\chi_{bJ}$ (J = 0, 1, 2) at $\sqrt{s}$ = 10.653, 10.701, 10.746, and 10.804 GeV, respectively. Here $\mathcal{L}$ is the integrated luminosity, $N^{\rm fit}$ is the sum of signal yields of $\Upsilon(1S) \to e^+e^-$ and $\Upsilon(1S) \to \mu^+\mu^-$ modes with purely statistical uncertainty, $N^{\rm UL}$ is the upper limit at 90% C.L. on the signal yield, $\varepsilon_{e^+e^-}$ and $\varepsilon_{\mu^+\mu^-}$ are reconstruction efficiencies for $\Upsilon(1S) \to e^+e^-$ and $\Upsilon(1S) \to \mu^+\mu^-$ modes, $\mathcal{B}^{\rm int}_{e^+e^-}$ and $\mathcal{B}^{\rm int}_{\mu^+\mu^-}$ are the product of the branching fractions of the intermediate states for $\Upsilon(1S) \to e^+e^-$ and $\Upsilon(1S) \to \mu^+\mu^-$ modes, $|1-\Pi|^2$ is the vacuum polarization factor, $1+\delta_{\rm ISR}$ is the radiative correction factor, syst is the systematic uncertainty, and $\sigma^{\rm UL}_{\rm Born}$ is the upper limit at 90% C.L. on the Born cross section.

$\sqrt{s}$ (GeV)	$\mathcal{L}$ (fb^{-1})	Channel	$N^{\rm fit}$	$N^{\rm UL}$	$\varepsilon_{e^+e^-}$	$\varepsilon_{\mu^+\mu^-}$	$\mathcal{B}^{\rm int}_{e^+e^-}$	$\mathcal{B}^{\rm int}_{\mu^+\mu^-}$	$\lvert1-\Pi\rvert^2$	$1+\delta_{\rm ISR}$	syst (%)	$\sigma^{\rm UL}_{\rm Born}$ (pb)
10.653	3.512	$\gamma\chi_{b0}$	-5.5 ± 4.9	8.5	0.215	0.361	0.00046	0.00048	0.930	0.901	15.5	9.18
		$\gamma\chi_{b1}$	10.4 ± 7.0	21.5	0.223	0.353	0.00841	0.00873	0.930	0.898	9.0	1.28
		$\gamma\chi_{b2}$	-0.7 ± 5.5	10.5	0.212	0.341	0.00430	0.00446	0.930	0.896	8.9	1.28
10.701	1.632	$\gamma\chi_{b0}$	-1.7 ± 2.8	7.0	0.214	0.346	0.00046	0.00048	0.931	0.905	15.5	16.68
		$\gamma\chi_{b1}$	-0.2 ± 3.7	8.6	0.217	0.351	0.00841	0.00873	0.931	0.903	9.0	1.11
		$\gamma\chi_{b2}$	-0.5 ± 3.4	8.0	0.219	0.341	0.00430	0.00446	0.931	0.901	8.9	2.06
10.746	9.818	$\gamma\chi_{b0}$	-2.9 ± 9.5	13.9	0.216	0.356	0.00046	0.00048	0.931	0.909	15.5	5.37
		$\gamma\chi_{b1}$	-6.1 ± 8.5	12.1	0.212	0.361	0.00841	0.00873	0.931	0.906	9.0	0.26
		$\gamma\chi_{b2}$	3.8 ± 9.7	19.1	0.218	0.358	0.00430	0.00446	0.931	0.904	8.9	0.79
10.804	4.689	$\gamma\chi_{b0}$	16.7 ± 8.1	30.1	0.222	0.361	0.00046	0.00048	0.932	0.914	15.5	23.77
		$\gamma\chi_{b1}$	-4.0 ± 5.6	10.0	0.224	0.366	0.00841	0.00873	0.932	0.911	9.0	0.43
		$\gamma\chi_{b2}$	-0.1 ± 5.7	11.2	0.228	0.364	0.00430	0.00446	0.932	0.909	8.9	0.94

We add individual uncertainties in quadrature to obtain the final uncertainties for $\mu^+\mu^-$ and e^+e^- modes related to the detection efficiency, which is 1.9%.

- Trigger simulation

We chose L1 CDC triggers of hie, c4, lml1, and ECL triggers of fyo, fy30, stt for our analysis. We study the uncertainty of these trigger bits by the Bhabha process and di-muon process. The efficiencies from data and MC are 99.8% and 99.6% for dimuon process, and 98.6% and 96.5% for Bhabha process. As a result, we include 0.2% uncertainty for $\mu\mu$ final state and 2.1% uncertainty for ee final state due to trigger simulation.

The above two sources of systematic uncertainties (Detection efficiency and Trigger simulation) for $\mu^+\mu^-$ and e^+e^- modes are different, thus we combine them to obtain the total systematic uncertainty by taking into account the detection efficiencies for $\mu^+\mu^-$ and e^+e^- modes as the weight factors.

- MC statistics

The statistical error in the MC efficiency can be calculated using $\Delta_\varepsilon = \sqrt{(\varepsilon(1-\varepsilon))/N}$, where ε is the reconstruction efficiency, and N is the total number of generated events. The uncertainty in the MC statistics is estimated by $\Delta_\varepsilon/\varepsilon$, which is 1.0%.

- Branching fractions of intermediate states

The uncertainties of branching fractions for $\chi_{b0} \to \gamma\Upsilon(1S), \chi_{b1} \to \gamma\Upsilon(1S), \chi_{b2} \to \gamma\Upsilon(1S), \Upsilon(1S) \to e^+e^-, \Upsilon(1S) \to \mu^+\mu^-$ are 13.9%, 5.7%, 5.6%, 4.6%, and 2.0%. The total uncertainties on branching fractions in $e^+e^- \to \gamma\chi_{b0}$, $e^+e^- \to \gamma\chi_{b1}$, and $e^+e^- \to \gamma\chi_{b2}$ are 14.6%, 7.3%, and 7.2%, respectively.

- Integrated luminosity

Belle II measures the luminosity at 1.2% precision using Bhabha, digamma, and mupair events [52].

- Angular distribution for $V \to \gamma\chi_{bJ}$ (J = 0, 1, 2)

We require the $|\cos(\theta_{\gamma_h})| < 0.7$ to suppress Bhabha background events. We change the uniform angular distribution to the distribution of $1 \pm \cos^2\theta$ for $V \to \gamma\chi_{bJ}$ (J = 0, 1, 2) and take the maximum difference of efficiency (4 %) as the uncertainty of different angular distributions.

- Beam-energy calibration

Table XI shows the measurements for the e^+e^- C.M. energy in data. We change the collision energies according to Table XI in the 4C kinematic fit and take the largest difference (C.M. energy(± uncertainty) relative to nominal C.M. energy) in efficiency as the uncertainty, which is less than 1%. We will take the difference of 1% in the signal efficiency as an uncertainty due to the beam-energy calibration.

TABLE XI. Measurement results for the energy of the scan data samples. [26]

point	Collected luminosity (fb^{-1})	E_{cm} (MeV)
1	3.521	10653.30 ± 0.71 ± 0.89 ± 0.50
2	1.633	10700.90 ± 0.61 ± 0.14 ± 0.50
3	9.818	10746.30 ± 0.46 ± 0.15 ± 0.50
4	4.690	10804.50 ± 0.65 ± 0.25 ± 0.50

- The radiative correction factor

To calculate the radiative correction factor of $e^+e^- \to \gamma\chi_{bJ}$ ($J = 0, 1, 2$), we assume the dressed cross section follows the $1/s$ line shape. We change the $1/s$ to $1/s^2$ [50] and take the difference on the radiative correction factor as the systematic uncertainty.

All the multiplicative uncertainties in the measurements of $\sigma_{\rm Born}(e^+e^- \to \gamma\chi_{bJ})$ are added in quadrature to obtain the total systematic uncertainty, which are summarized in Table XII.

- signal PDF parameters

We considered the following systematic uncertainties associated with the signal PDF parameters. We varied the mean of the signal PDF according to the uncertainties of the χ_{bJ} masses from Particle Data Group [43], which are ± 0.42 MeV, ± 0.26 MeV, and ± 0.26 MeV for χ_{b0}, χ_{b1}, and χ_{b2}, respectively. To account for data-simulation discrepancies, the photon energy in simulated events is smeared according to the measured photon energy resolution scale factor, 1.01 ± 0.01, obtained from the $\pi^0 \to \gamma\gamma$ control sample [51]. We repeated the fit while varying the photon energy resolution scale factor within its uncertainty.

TABLE XII. Relative multiplicative systematic uncertainties of the measurements of the Born cross sections for $e^+e^- \to \gamma\chi_{bJ}$ ($J = 0, 1, 2$) at $\sqrt{s} = 10.653$, 10.701, 10.746, and 10.804 GeV, respectively.

Sources	$\gamma\chi_{b0}$	$\gamma\chi_{b1}$	$\gamma\chi_{b2}$
Branching fractions	14.6	7.3	7.2
Detection efficiency	1.9	1.9	1.9
Trigger simulation	1.7	1.7	1.7
MC statistics	1.0	1.0	1.0
Integrated luminosity	1.2	1.2	1.2
Angular distributions	3.9	3.9	4.0
Beam-energy calibration	1.0	1.0	1.0
Radiative correction factor	1.5	1.4	1.4
Sum	15.5	9.0	8.9

- Fit model

The systematic uncertainties associated with the fitting procedure are estimated by changing the order of the background polynomial and the range of the fit, and comparing the fit results without a χ_{b0} component due to the small branching fraction for $\chi_{b0} \to \gamma\Upsilon(1S)$.

In the calculations of upper limits, the systematic uncertainties are taken into account in two steps. First, when we study the additive systematic uncertainty from from the signal PDF parameters and fit model (as described above), we calculate the upper limit for each possible case and take the most conservative upper limit at 90% C.L. on the number of signal events. Then, the likelihood with the most conservative upper limit is convolved with a Gaussian function whose width is equal to the corresponding total multiplicative uncertainty.

5. SUMMARY

In summary, we report a search for the $e^+e^- \to \gamma\chi_{bJ}$ ($J = 0, 1, 2$) processes at $\sqrt{s} =$ 10.653, 10.701, 10.746 and 10.804 GeV. We do not find evidence for any process, and set upper limits at 90% C.L. on the corresponding Born cross sections.

The upper limit at 90% C.L. on the Born cross section for $e^+e^- \to \gamma\chi_{b1}$ at $\sqrt{s} = 10.746$ GeV is 0.26 pb. This value is significantly smaller than the values of (3.6 ± 0.9) pb and (1.4 ± 0.2) pb for $e^+e^- \to \omega\chi_{b1}$ and $e^+e^- \to \pi^+\pi^-\Upsilon(2S)$ at $\sqrt{s} = 10.746$ GeV [6, 24]. Interpretations as an admixture of the conventional $4S$ and $3D$ states predict comparable branching fractions of 10^{-3} for $\Upsilon(10753) \to \omega\chi_{b1}$ and $\Upsilon(10753) \to \pi^+\pi^-\Upsilon(2S)$ [7, 8]. Therefore, the branching fraction for $\Upsilon(10753) \to \gamma\chi_{b1}$ is less than 10^{-3}. If the $\Upsilon(10753)$ consists of a significant D-wave component, the branching fraction for $\Upsilon(10753) \to \gamma\chi_{b1}$ can reach the magnitude of 10^{-2} [28, 29]. Therefore, our measurement indicates that the D-wave component in the $\Upsilon(10753)$ cannot be large.

---

* 22210200014@m.fudan.edu.cn

† jiasen@seu.edu.cn

‡ shencp@fudan.edu.cn

[1] M. Artuso *et al.* [CLEO], Phys. Rev. Lett. **94** (2005), 032001 doi:10.1103/PhysRevLett.94.032001 [arXiv:hep-ex/0411068 [hep-ex]].

[2] D. Besson *et al.* [CLEO], Phys. Rev. D **74** (2006), 012003 doi:10.1103/PhysRevD.74.012003 [arXiv:hep-ex/0512061 [hep-ex]].

[3] M. Abumusabh *et al.* [Belle-II], [arXiv:2508.16036 [hep-ex]].

[4] B. G. Fulsom *et al.* [Belle], Phys. Rev. Lett. **121** (2018) no.23, 232001 doi:10.1103/PhysRevLett.121.232001 [arXiv:1807.01201 [hep-ex]].

[5] R. Mizuk *et al.* (Belle Collaboration), JHEP **10**, 220 (2019).

[6] I. Adachi *et al.* (Belle II Collaboration), arXiv:2401.12021.

[7] Z.Y. Bai, Y.S. Li, Q. Huang, X. Liu, and T. Matsuki, Phys. Rev. D **105**, 074007 (2022).

[8] Y.S. Li, Z.Y. Bai, Q. Huang, and X. Liu, Phys. Rev. D **104**, 034036 (2021).

[9] Q. Li, M.S. Liu, Q.F. Lü, L.C. Gui, and X.H. Zhong, Eur. Phys. J. C **80**, 59 (2020).

[10] B. Chen, A.L. Zhang, and J. He, Phys. Rev. D **101**, 014020 (2020).

[11] J.F. Giron and R.F. Lebed, Phys. Rev. D **102**, 014036 (2020).

[12] V. Kher, R. Chaturvedi, N. Devlani, and A.K. Rai, Eur. Phys. J. Plus **137**, 357 (2022).

[13] Y.S. Li, Z.Y. Bai, and X. Liu, Phys. Rev. D **105**, 114041 (2022).

[14] W.H. Liang, N. Ikeno, and E. Oset, Phys. Lett. B **803**, 135340 (2020).

[15] N.Hüsken, R.E. Mitchell, and E.S. Swanson, Phys. Rev. D **106**, 094013 (2022).

[16] E.V. Beveren and G. Rupp, Prog. Part. Nucl. Phys. **117**, 103845 (2021).

[17] J.T. Castellà and E. Passemar, Phys. Rev. D **104**, 034019 (2021).

[18] N. Brambilla, S. Eidelman, C. Hanhart, A. Nefediev, C.P. Shen, C.E. Thomas, A. Vairo, and C.Z. Yuan, Phys. Rept. **873**, 1 (2020).

[19] A. Ali, L. Maiani, A.Y. Parkhomenko, and W. Wang, Phys. Lett. B **802**, 135217 (2020).

[20] P. Bicudo, N. Cardoso, L. Müller, and M. Wagner, Phys. Rev. D **103**, 074507 (2021).

[21] P. Bicudo, N. Cardoso, L. Müller, and M. Wagner, Phys. Rev. D **107**, 094515 (2023).

[22] Z. G. Wang, Chin. Phys. C **43**, 123102 (2019).

[23] A.Y. Parkhomenko and W. Wang, Phys. Part. Nucl. Lett. **20**, 381 (2023).
[24] I. Adachi *et al.* (Belle II Collaboration), Phys. Rev. Lett. **130**, 091902 (2023).
[25] X.H. He *et al.* (Belle Collaboration), Phys. Rev. Lett. **113**, 142001 (2014).
[26] I. Adachi *et al.* [Belle-II], [arXiv:2405.18928 [hep-ex]].
[27] I. Adachi *et al.* (Belle II Collaboration), Phys. Rev. D **109**, 072013 (2024).
[28] S. Godfrey and K. Moats, Phys. Rev. D **92**, 054034 (2015).
[29] J.Z. Wang, Z.F. Sun, X. Liu, and T. Matsuki, Eur. Phys. J. C **78**, 915 (2018).
[30] M. Ablikim *et al.* (BESIII Collaboration), Phys. Rev. Lett. **118**, 092001 (2017).
[31] M. Ablikim *et al.* (BESIII Collaboration), Chin. Phys. C **39**, 041001 (2015).
[32] D. Santel *et al.* (Belle Collaboration), Phys. Rev. D **93**, 011101 (2016).
[33] S. Actis *et al.* (Working Group on Radiative Corrections and Monte Carlo Generators for Low Energies Collaborations), Eur. Phys. J. C **66**, 585 (2010).
[34] E.A. Kuraev and V.S. Fadin, Yad. Fiz. **41**, 733 (1985) [Sov. J. Nucl. Phys. **41**, 466 (1985)].
[35] S. Jadach, B.F.L. Ward, and Z. W*c* as, Phys. Rev. D **63**, 113009 (2001); Comput. Phys. Commun. **130**, 260 (2000).
[36] M. Benayoun, S.I. Eidelman, V.N. Ivanchenko, and Z.K. Silagadze, Mod. Phys. Lett. A **14**, 2605 (1999).
[37] G. Rodrigo, H. Czyż, J. H. Kühn and M. Szopa, Eur. Phy. J. C **24**, 71 (2002).
[38] D.J. Lange, Nucl. Instr. and Methods Phys. Res. Sect. A **462**, 152 (2001).
[39] S. Agostinelli *et al.*, Nucl. Instrum. Meth. A **506**, 250 (2003).
[40] Please see details via this link: https://cdbweb.sdcc.bnl.gov/GlobalTag?id=2483.
[41] G. Punzi, eConf C030908, MODT002 (2003).
[42] T. Skwarnicki, Ph.D. thesis, Institute for Nuclear Physics, 1986; DESY Report No. DESY F31-86-02, 1986.
[43] R.L. Workman *et al.* (Particle Data Group), Prog. Theor. Exp. Phys. **2022**, 083C01 (2022) and 2023 update.
[44] A. Glazov, P. Rados, A. Rostomyan, E. Paoloni, and L. Zani, BELLE2-NOTE-PH-2020-006.
[45] D. Ferlewicz, M. Milesi, and P. Rocchetti, BELLE2-NOTE-PH-2020-010.
[46] A. Martini and A.N. Charan, BELLE2-NOTE-TE-2020-003.
[47] S. Yo, K. Uno, and S. Yo, BELLE2-NOTE-PH-2019-043.
[48] J. Skorupa, BELLE2-NOTE-TE-2019-016.
[49] Lu Cao and K. Tackmann, BELLE2-NOTE-TE-2024-002.
[50] S. Jia *et al.* (Belle Collaboration), Phys. Rev. D **98**, 092015 (2018).
[51] Q.P. Ji, S. Jia, and C.P. Shen, BELLE2-NOTE-PH-2021-021.
[52] I. Adachi *et al.* (Belle II Collaboration), arXiv:2407.00965.